Mechanics Research Communications 111 (2021) 103660

Contents lists available at ScienceDirect

Mechanics Research Communications

journal homepage: www.elsevier.com/locate/mechrescom

Dynamic response of deep-water catenary risers made of functionally graded materials

J.C.R. Albino[a,*], C.A. Almeida[b], I.F.M. Menezes[b], G.H. Paulino[c]

[a] Deparment of Mechanical Engineering, SENAI CIMATEC, BA 41650-010, Brazil
[b] Deparment of Mechanical Engineering, Pontifical Catholic University of Rio de Janeiro, RJ 22453-900, Brazil
[c] School of Civil and Environmental Engineering, Georgia Institute of Technology, Atlanta, GA 30332, USA

ARTICLE INFO

Article history:
Received 6 October 2019
Revised 29 December 2020
Accepted 1 January 2021
Available online 7 January 2021

Keywords:
Functionally graded material
Steel catenary riser
Finite element
Nonlinear dynamic analysis

ABSTRACT

This paper examines the structural behavior of a steel catenary riser (SCR) with a segment composed of a functionally graded material (FGM) at the touchdown zone (TDZ). A co-rotational beam formulation is employed to evaluate the influence of material gradation on the static and dynamic nonlinear behavior of the riser. A finite element model is developed to predict the riser response considering environmental and operational conditions such as self-weight, buoyancy, current, soil contact, waves, buoys, and ship motion. Moreover, a comparison of SCR configurations is made between those constructed from FGM and those constructed from standard homogeneous materials. The study indicates that an SCR configuration with an incorporated FGM segment improves the curvatures near the TDZ, where designing to mitigate fatigue damage is critical.

1. Introduction

Riser technologies constantly face new challenges imposed by the recent deep- and ultra-deep-water oil discoveries and the associated harsh environmental conditions. Compared to other riser configurations, steel catenary risers (SCRs) are attractive owing to their simplicity, reliability, and cost effectiveness. Moreover, SCRs are resistant to high pressures and temperatures, and thus larger diameter models can be deployed more successfully when compared to flexible risers [1].

The dynamic representation of SCRs requires nonlinear numerical models owing primarily to the significant motion experienced at the hang-off point, fluid drag loadings, and riser-seabed interaction. To study the effect of these nonlinearities in the global dynamic response of the riser, finite element approaches have been extensively reported in the literature [2–9].

There are two main concerns in the design of catenary risers for applications in deep-water conditions: a) the fatigue damage assessment at the points of the riser that touch the seabed, known as the touchdown zone (TDZ) [10]. This problem is influenced by the cyclic riser-seabed interaction in the TDZ and is dependent on the seabed stiffness and damping characteristics [11–13]; and b) the risk of riser corrosion due to the presence of corrosive contaminants (CO_2 and H_2S) in the fluid (oil) [14,15].

The use of composite materials in riser applications has increased recently due to the potential advantages that they offer over metallic risers, including their high stiffness-to-weight ratio, high tensile and fatigue strength, improved structural damping, low thermal conductivity, acceptable corrosion resistance, and low maintenance requirements [16,17]. However, delamination is the most common failure associated with composite risers, as has been reported in numerous research studies [18–20]. Unlike traditional composite materials, functionally graded materials (FGMs) present a smooth and gradual compositional variation with no sharp interfaces, thus eliminating the possibility of classical delamination. Typical FGMs, of interest in this study, are a mixture of ceramic and metal, aiming to combine the best properties of each phase, such as the hardness and corrosion resistance of the ceramic phase, and the toughness, machinability, and weldability of the metallic phase [21,22]. Owing to their unique properties, FGMs are promising materials for application in risers such as SCRs under deep-water conditions. In this context, and under the assumption that the FGM is available at the engineering scale of interest, then they could be applied in the TDZ to improve the SCR fatigue performance as a potential alternative solution to the concept of weight-distributed SCRs [23–26].

As a proof of concept, the use of an SCR with an FGM segment at the TDZ is proposed (as illustrated in Fig. 1). The static and dynamic nonlinear behavior of the riser is evaluated using a recently

* Corresponding author.
E-mail addresses: jc.romeroal@outlook.com (J.C.R. Albino), calmeida@puc-rio.br (C.A. Almeida), ivan@puc-rio.br (I.F.M. Menezes), paulino@gatech.edu (G.H. Paulino).

https://doi.org/10.1016/j.mechrescom.2021.103660
0093-6413/

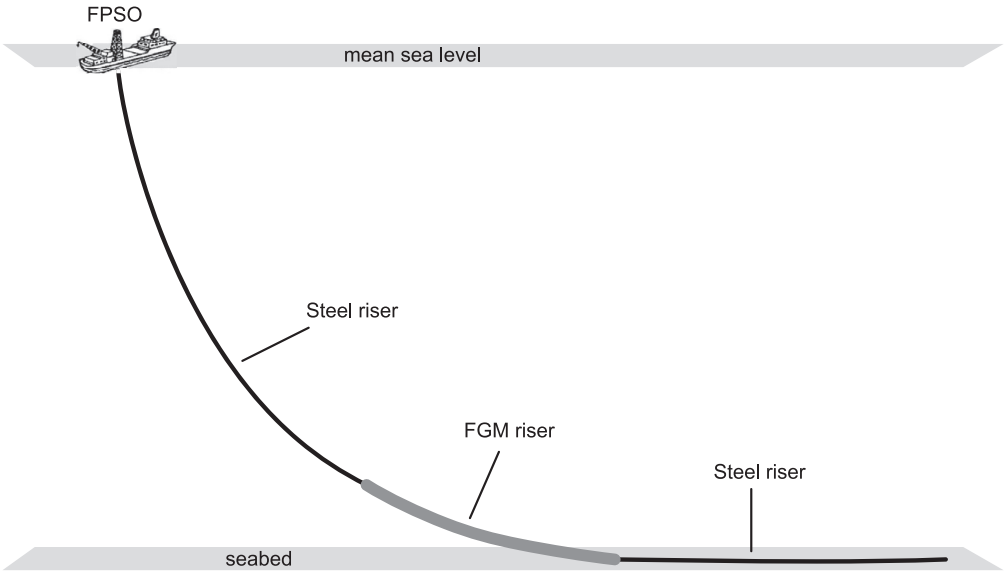

Fig. 1. Schematic of SCR FGM concept.

proposed co-rotational formulation [9]. The results obtained herein demonstrate that this new FGM SCR riser approach leads to a significant reduction in the riser curvature at the TDZ. Hence, it could be applied to SCRs in harsh environmental conditions where, in addition to controlling the dynamic stresses, the use of FGMs could help prevent collateral problems such as corrosion and the formation of paraffin deposits.

2. Finite element formulation

In this section, a short review of the finite element formulation for nonlinear dynamic analysis of FGM risers, as proposed in [9], is presented. Using the principle of virtual work (PVW), the static equilibrium condition of the riser at time (t+Δt), for an updated Lagrangian formulation [27], is given by

$$\int_{tV} {}_t^{t+\Delta t}S_{ij}\delta {}_t^{t+\Delta t}\varepsilon_{ij} d^tV = \int_{0S} {}_0^{t+\Delta t}f_i^S \delta u_i^S d^0S + \int_{0V} {}_0^{t+\Delta t}f_i^B \delta u_i d^0V \quad (1)$$

where ${}_t^{t+\Delta t}S_{ij}$ is the second Piola-Kirchhoff stress tensor, ${}_t^{t+\Delta t}\varepsilon_{ij}$ is the Green-Lagrange strain tensor, ${}_0^{t+\Delta t}f_i^S$ is the surface force, ${}_0^{t+\Delta t}f_i^B$ is the body force, and δu_i is the virtual displacement vector component.

The PVW can be extended to dynamic problems using the D'Alembert principle [28]. Therefore, by incorporating inertia and viscous damping into Eq. (1), the incremental equation of dynamic equilibrium is obtained as

$$\begin{aligned}&\int_{0V} {}^0\rho^{t+\Delta t}\ddot{u}_i\delta u_i d^0V + \int_{0V} k^{t+\Delta t}\dot{u}_i\delta u_i d^0V + \int_{tV} {}_tC_{ijrs}\Delta e_{rs}\delta\Delta e_{ij} d^tV\\ &+ \int_{tV} {}^t\tau_{ij}\delta\Delta\eta_{ij} d^tV = \int_{0S} {}_0^{t+\Delta t}f_i^S\delta u_i^S d^0S + \int_{0V} {}_0^{t+\Delta t}f_i^B\delta u_i d^0V\\ &- \int_{tV} {}^t\tau_{ij}\delta\Delta e_{ij} d^tV \end{aligned} \quad (2)$$

After the discretization of the riser using beam element kinematics, the global dynamic equilibrium equation can be written in the matrix form in terms of the incremental nodal displacements ($\mathbf{\Delta U}$), updated nodal accelerations ($\ddot{\mathbf{U}}$), and velocities ($\dot{\mathbf{U}}$) as

$$\mathbf{M}^{t+\Delta t}\ddot{\mathbf{U}} + \mathbf{D}^{t+\Delta t}\dot{\mathbf{U}} + \left({}_t^t\mathbf{K_L} + {}_t^t\mathbf{K_{NL}}\right)\mathbf{\Delta U} = {}^{t+\Delta t}\mathbf{R} - {}_t^t\mathbf{F} \quad (3)$$

where $\mathbf{M}$, $\mathbf{D}$, ${}_t^t\mathbf{K_L}$, ${}_t^t\mathbf{K_{NL}}$, ${}^{t+\Delta t}\mathbf{R}$ and ${}_t^t\mathbf{F}$ represent the global mass matrix, global damping matrix, global linear incremental stiffness matrix, global nonlinear geometric stiffness matrix, updated global vector of the external nodal forces, and global vector of internal nodal forces, respectively, which can be expressed as

$$\begin{aligned}\mathbf{M} &= \sum_m \int_{0V^{(m)}} {}^0\rho^{(m)}\mathbf{H}^{(m)T}\mathbf{H}^{(m)} d^0V^{(m)},\\ \mathbf{D} &= \sum_m \int_{0V^{(m)}} {}^0k^{(m)}\mathbf{H}^{(m)T}\mathbf{H}^{(m)} d^0V^{(m)},\\ {}_t^t\mathbf{K_L} &= \sum_m \int_{tV^{(m)}} {}_t^t\mathbf{B_L^{(m)}}^T {}_t\mathbf{C}^{(m)} {}_t^t\mathbf{B_L^{(m)}} d^tV^{(m)},\\ {}_t^t\mathbf{K_{NL}} &= \sum_m \int_{tV^{(m)}} {}_t^t\mathbf{B_{NL}^{(m)}}^T {}_t\boldsymbol{\tau}^{(m)} {}_t^t\mathbf{B_{NL}^{(m)}} d^tV^{(m)},\\ {}^{t+\Delta t}\mathbf{R} &= \sum_m \int_{0S^{(m)}} \mathbf{H}^{S(m)T} {}_0^{t+\Delta t}\mathbf{f}^{S(m)} d^0S^{(m)}\\ &\quad + \sum_m \int_{0V^{(m)}} \mathbf{H}^{(m)T} {}_0^{t+\Delta t}\mathbf{f}^{B(m)} d^0V^{(m)},\\ {}_t^t\mathbf{F} &= \sum_m \int_{tV^{(m)}} {}_t^t\mathbf{B_L^{(m)}}^T {}_t\hat{\boldsymbol{\tau}}^{(m)} d^tV^{(m)}\end{aligned} \quad (4)$$

Here, $\mathbf{H}^{(m)}$ is the m-element interpolation matrix (for further information on these matrices see [9]).

The material gradation throughout the riser thickness is included in the constitutive matrix ($\mathbf{C}$) and the mass matrix ($\mathbf{M}$). Thus, we use a nonhomogeneous material model where the elastic modulus (E) and density (ρ) vary according to a power law along the radial coordinate through the riser thickness (r), as follows:

$$E = E_o(r/r_o)^a, \quad \rho = \rho_o(r/r_o)^b, \quad r_i \le r \le r_o \quad (5)$$

where a and b are the non-homogeneity parameters of the Young's modulus and material density, respectively, r_i is the riser internal radius, and r_o is the riser outer radius.

In Eq. (3), a Newmark time integration scheme is used to express the displacements, velocities, and accelerations at time $(t+\Delta t)$ in terms of the known variables at time t. Thus,

$$\begin{aligned}{}^{t+\Delta t}\ddot{\mathbf{U}} &= \frac{1}{\beta\Delta t^2}\mathbf{\Delta U} - \frac{1}{\beta\Delta t}{}^t\dot{\mathbf{U}} - \left(\frac{1}{2\beta} - 1\right){}^t\ddot{\mathbf{U}}\\ {}^{t+\Delta t}\dot{\mathbf{U}} &= {}^t\dot{\mathbf{U}} + \Delta t(1-\gamma){}^t\ddot{\mathbf{U}} + \gamma\Delta t{}^{t+\Delta t}\ddot{\mathbf{U}}\\ {}^{t+\Delta t}\mathbf{U} &= {}^t\mathbf{U} + \mathbf{\Delta U}\end{aligned} \quad (6)$$

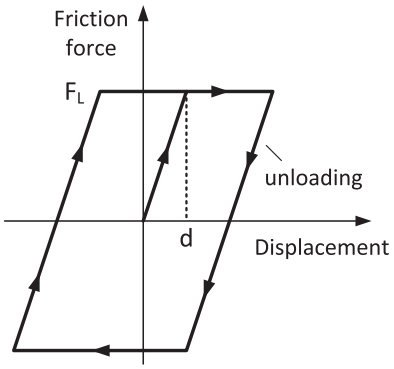

Fig. 2. Simplified riser-soil friction model.

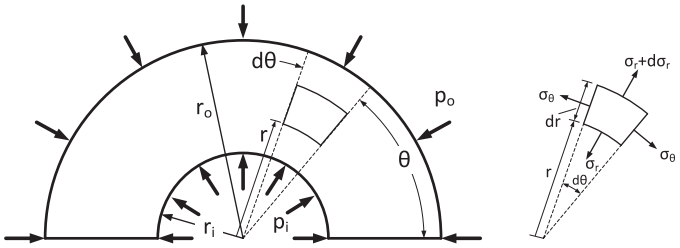

Fig. 3. Thick-walled FGM cylinder.

where Δt is the time step. In this work, the Hilber, Hughes and Taylor (HHT) algorithm [29] is used, where β and γ are constants defined as

$$\beta = \frac{1}{4}(1-\alpha)^2 \quad \text{and} \quad \gamma = \frac{1}{2} - \alpha, \quad -1/3 \leq \alpha \leq 0 \tag{7}$$

The external forces considered in this study are the effect of the self-weight, buoyancy, hydrodynamic loads (due to maritime waves, currents, and added mass inertia), prescribed displacements at the floating unit, and forces exerted by the floaters (for further details, see [7]).

The riser-soil interaction is modeled by associating bilinear springs to all the nodes in the structure. Whenever a node, in its deformed position, comes into contact with the soil, the soil stiffness k_s is activated. The friction force due to the riser-soil contact is represented by an idealized elastoplastic formulation that allows the consideration of anisotropic friction, with the definition of different soil friction coefficients for the axial and lateral directions of the riser μ_a and μ_l, respectively. The complete interaction (coupled model) between the friction forces in these directions follows the formulation presented in Reference [30]. The elastoplastic behavior of the friction force is illustrated in Fig. 2, where $F_L = \mu$ N and d are the limits of friction force and displacement that define the elastic behavior; μ is the friction coefficient; and N is the normal contact force. For further details about the equations that govern the riser-soil interaction, we refer the reader to the work of Silva et al. [30].

3. Stress evaluation in functionally graded risers

This section presents the details of the stress analysis of the FGM risers used in the present study. The references of interest are [31–33].

3.1. Stresses due to internal and external pressures in thick-walled FGM cylinders

The exact solution for stress distribution in thick-walled FGM cylinders under internal pressure p_i and external pressure p_o is presented. This problem was originally solved by Tutuncu and Ozturk [31]; however, they only considered the effect of internal pressure. The FGM model is isotropic with a constant Poisson's ratio (v), and the Young's modulus (E) varies according to the power law displayed in Eq. (5).

Considering a cylindrical coordinate system (r, θ, x), and axisymmetry about the x-axis (along the axial direction), the differential equation of the stress equilibrium in the radial direction can be written as [32]

$$\frac{d\sigma_r}{dr} + \frac{\sigma_r - \sigma_\theta}{r} = 0 \tag{8}$$

where σ_r and σ_θ are the radial and circumferential stresses of the cylinder, respectively. An illustration of the thick-walled FGM cylinder is presented in Fig. 3.

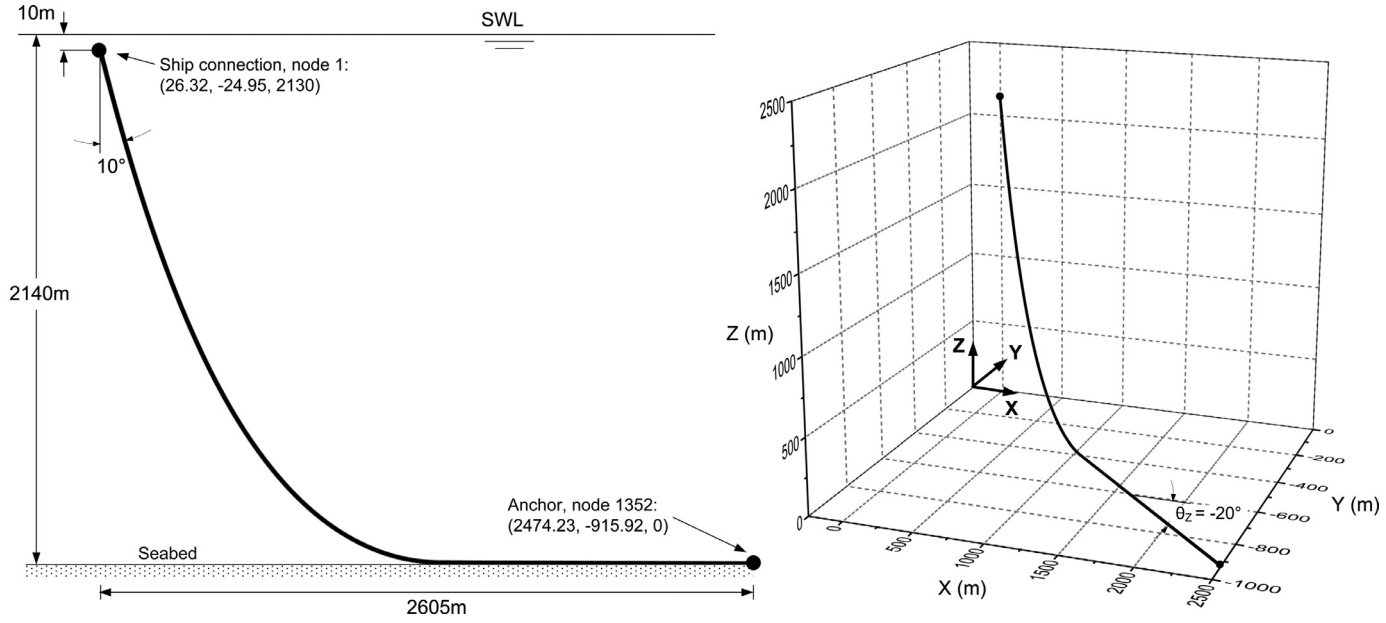

Fig. 4. Steel catenary riser.

Table 1
Steel catenary data.

Total length of riser, L	4053 m	**Homogeneous material (Steel):**	
External diameter, D_o	0.219 m	Young's modulus	E = 207 GPa
Internal diameter, D_i	0.175 m	Specific weight	γ = 77 kN/m^3
Morison's inertia coefficient, C_m	2.0	Poisson's ratio	ν = 0.3
Morison's drag coefficient, C_D	1.0	**Functionally graded material (Ni_3Al-TiC):**	
Floater's weight	0.453 kN/m	Young's modulus	$E(r) = 420.7\ (r/r_o)^{3.126}$ GPa
Floater's buoyancy force	0.628 kN/m	Specific weight	$\gamma(r) = 49.2\ (r/r_o)^{-1.85}$ kN/m^3
Specific weight of internal fluid	6 kN/m^3	Poisson's ratio	ν = 0.3
Specific weight of sea water	10.055 kN/m^3	**Soil parameters:**	
		Axial elastic deflection limit, d_a	0.030 m
		Lateral elastic deflection limit, d_l	0.219 m
		Axial soil resistance coefficient, μ_a	1.54
		Lateral soil resistance coefficient, μ_l	1.63
		Soil stiffness, k_s	1269 kN/m

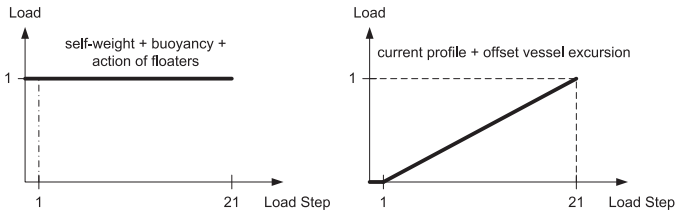

Fig. 5. Static loading characteristics.

Table 2
Static environmental loads.

Current profile:		
Depth (m)	Speed (m/s)	θ_z
0.0	1.57	180
1.0	1.57	180
4.5	1.53	180
40.0	1.39	180
340.0	0.41	180
740.0	0.29	270
1140.0	0.29	225
1540.0	0.29	225
1940.0	0.38	225
2140.0	0.00	225
Offset vessel excursion (m):		
Displacement in the x-direction, -138.4		
Displacement in the y-direction, 57.3		

Assuming a state of plane strain ($\varepsilon_z = 0$), and using the strain-displacement relations for small strains, together with the generalized Hooke's law, the stress-displacement relationships are given by

$$\sigma_r = \frac{E_o(r/r_o)^a}{(1+\nu)(1-2\nu)}\left[(1-\nu)\frac{du_r}{dr} + \nu\frac{u_r}{r}\right] \tag{9}$$

$$\sigma_\theta = \frac{E_o(r/r_o)^a}{(1+\nu)(1-2\nu)}\left[\nu\frac{du_r}{dr} + (1-\nu)\frac{u_r}{r}\right] \tag{10}$$

Substituting Eqs. (9) and (10) into Eq. (8), we obtain the governing differential equation for the radial displacement u_r, i.e.,

$$r^2u_r'' + (a+1)ru_r' + (\nu^*a - 1)u_r = 0 \tag{11}$$

where $\nu^* = \nu/(1-\nu)$.

A standard solution for Eq. (11) is $u_r = r^m$, where m is a constant. Substituting this solution into Eq. (11) we obtain the characteristic equation $m^2 + am + (\nu^*a - 1) = 0$, whose roots are

$$m_1 = \frac{1}{2}\left(-a - \sqrt{a^2 - 4(\nu^*a - 1)}\right),$$
$$m_2 = \frac{1}{2}\left(-a + \sqrt{a^2 - 4(\nu^*a - 1)}\right) \tag{12}$$

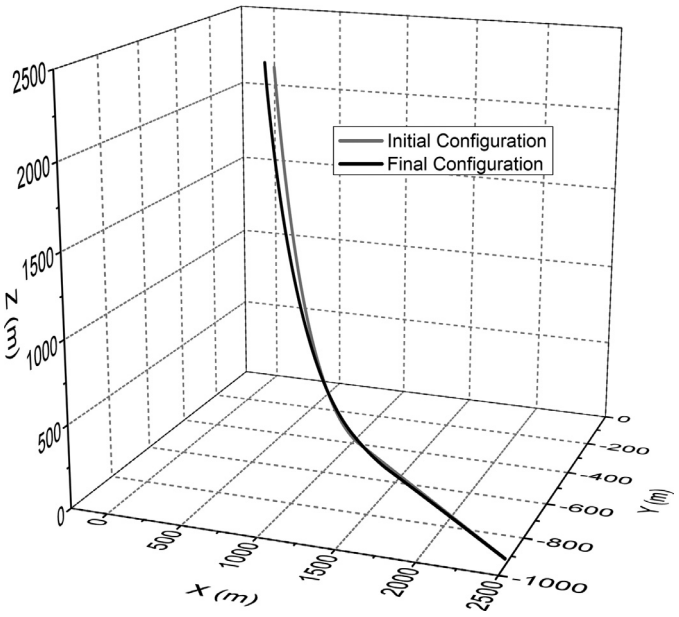

Fig. 6. Static riser configurations.

Table 3
Prescribed motions at riser's top connection.

DOF	Amplitude	Phase (deg)	Period (s)
U_X	1.025 m	56.886	13.242
U_Y	3.054 m	93.042	13.242
U_Z	10.794 m	329.870	13.242
θ_X	7.678°	302.750	13.242
θ_Y	1.251°	230.010	13.242
θ_Z	1.191°	176.240	13.242

Table 4
Minimum values of radius of curvature (in meters).

Time interval	30–37s	43–50s	57–63s
Homogeneous riser	17.21m	18.90m	15.65m
FGM riser	26.74m (+55.4%)	26.90m (+42.3%)	26.94m (+72.1%)

For typical numerical values of a and ν^* (where a, $\nu^* \in \Re$), distinct roots are considered. Therefore, a general solution for u_r is obtained as

$$u_r = C_1 r^{m_1} + C_2 r^{m_2} \tag{13}$$

Using the stress boundary conditions $\sigma_r(r_i) = -p_i$ and $\sigma_r(r_o) = -p_o$, constants C_1 and C_2 are obtained, and thus we obtain the re-

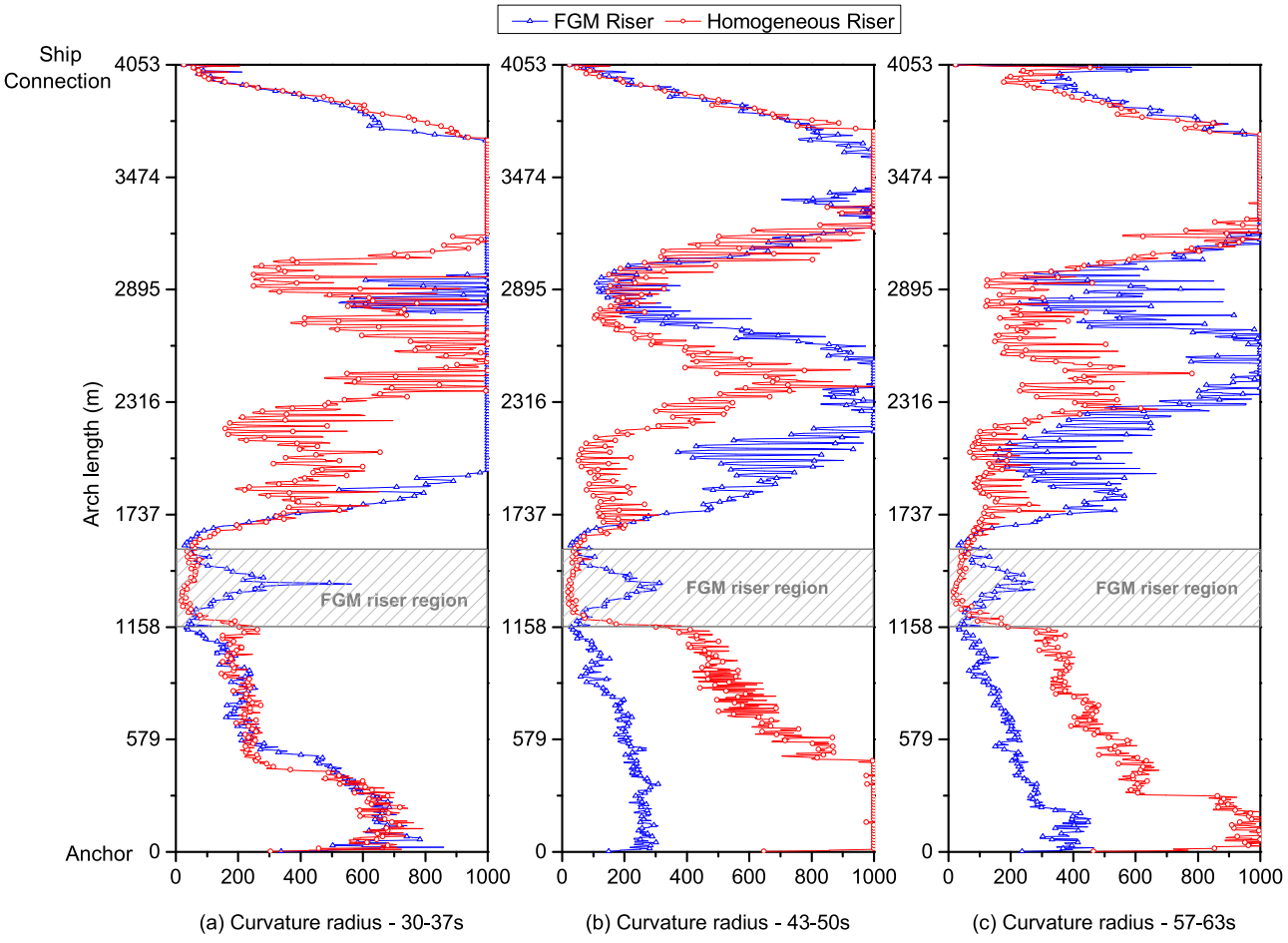

Fig. 7. Envelope of radii of curvature for different time intervals.

Table 5
Nodes with smallest curvature radius obtained from riser analyses.

Time interval	30–37*s*	43–50*s*	57–63*s*
Homogeneous riser	920	906	904
FGM riser	968	825	968

sulting stresses:

$$\sigma_r = \frac{(r/r_o)^{a-1}}{(r_i/r_o)^{m_1} - (r_i/r_o)^{m_2}} \left\{ -\left[p_i \left(\frac{r_i}{r_o}\right)^{1-a} - p_o \left(\frac{r_i}{r_o}\right)^{m_2} \right] \left(\frac{r}{r_o}\right)^{m_1} + \left[p_i \left(\frac{r_i}{r_o}\right)^{1-a} - p_o \left(\frac{r_i}{r_o}\right)^{m_1} \right] \left(\frac{r}{r_o}\right)^{m_2} \right\} \tag{14}$$

$$\sigma_\theta = \frac{(r/r_o)^{a-1}}{(r_i/r_o)^{m_1} - (r_i/r_o)^{m_2}} \left\{ -\left[\frac{\nu m_1 + (1-\nu)}{\nu + (1-\nu) m_1} \right] \times \left[p_i \left(\frac{r_i}{r_o}\right)^{1-a} - p_o \left(\frac{r_i}{r_o}\right)^{m_2} \right] \left(\frac{r}{r_o}\right)^{m_1} + \left[\frac{\nu m_2 + (1-\nu)}{\nu + (1-\nu) m_2} \right] \left[p_i \left(\frac{r_i}{r_o}\right)^{1-a} - p_o \left(\frac{r_i}{r_o}\right)^{m_1} \right] \left(\frac{r}{r_o}\right)^{m_2} \right\} \tag{15}$$

3.2. Von Mises equivalent stress

To determine the axial stress to which a submerged FGM riser is subjected, an approach based on [33] is used. The superposition principle is adopted considering the resulting axial stress σ_x as the sum of the stresses caused by the real axial force, F_x, and the bending moments, M_y and M_z. Thus,

$$\sigma_x = E(r) \left(\frac{F_x}{\overline{EA}} - \frac{M_z y}{\overline{EI}} + \frac{M_y z}{\overline{EI}} \right) \tag{16}$$

where the expressions of the equivalent structural rigidities $\overline{EA}$ and $\overline{EI}$ are given in [9], and y and z are the local coordinates of a point defined within the riser thickness $\left(r_i \le \sqrt{y^2 + z^2} \le r_o \right)$, with r_i and r_o being the inner and outer radii, respectively.

Defining $M_R = \sqrt{M_y^2 + M_z^2}$ as the resulting bending moment, the axial stress may assume the following two extreme values:

$$\sigma_{x1} = E(r) \left(\frac{F_x}{\overline{EA}} + \frac{M_R r}{\overline{EI}} \right) \quad \text{and} \quad \sigma_{x2} = E(r) \left(\frac{F_x}{\overline{EA}} - \frac{M_R r}{\overline{EI}} \right) \tag{17}$$

Thus, the von Mises equivalent stress, σ_{vM}, along the riser can be expressed as

$$\sigma_{vM} = \max \left\{ \begin{matrix} \frac{1}{2} \left((\sigma_r - \sigma_\theta)^2 + (\sigma_r - \sigma_{x1})^2 + (\sigma_{x1} - \sigma_\theta)^2 \right)^{1/2} \\ \frac{1}{2} \left((\sigma_r - \sigma_\theta)^2 + (\sigma_r - \sigma_{x2})^2 + (\sigma_{x2} - \sigma_\theta)^2 \right)^{1/2} \end{matrix} \right\} \tag{18}$$

where the radial (σ_r) and circumferential (σ_θ) stresses are defined by Eqs. (9) and (10), respectively.

In Eq. (18), the shear stresses are neglected according to the Euler-Bernoulli beam model adopted in this work. This approach is more appropriate to model slender structures such as risers [33].

4. Case study

This example presents a real case scenario of an SCR, 4053 m in length, submerged to a depth of 2140 m. The upper end of

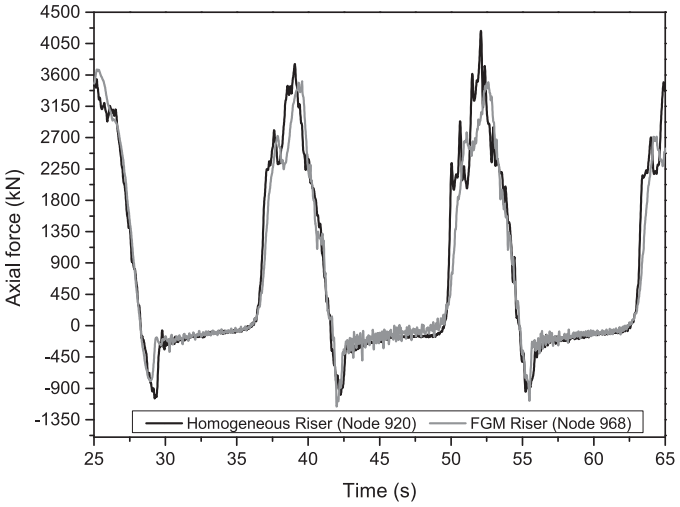

Fig. 8. Time history of the axial force in typical node within the TDZ.

the riser was connected to a floating production vessel 10 m below the still water level (SWL) with a hang-off angle of 10°; the other end was anchored onto the seabed, as indicated in Fig. 4. The catenary's plane was located at a 20° angle with respect to the global XZ plane. The initial deformed configuration considered a simple catenary with stiffness along its axial direction and under self-weight and buoyancy forces. The solution was obtained by integrating the differential equation of equilibrium of an elastic cable. Using this initial configuration, as illustrated in Fig. 4, static and dynamic loads were then applied. The riser was modeled using 1351 equally long beam elements; the physical and geometric properties, and the characteristics of the riser-seabed interaction, are presented in Table 1.

Static and dynamic analyses were performed considering the following effects: current, self-weight, forces exerted by the floaters, static vessel offset, and prescribed displacements at the top of the connection due to wave action. In the first analysis, the riser was made entirely of steel with a specific weight $77\,kN/m^3$ and a modulus of elasticity of $207\,GPa$. For the static analysis, the loadings were applied in 21 steps as illustrated in Fig. 5. In the first step, only the self-weight and floaters were considered; in the next 20 steps, a vessel offset of $150\,m$ (corresponding to 7% of the water depth) and the current load were applied. The current profile data and vessel offset are given in Table 2. The current direction (θ_z) is measured counterclockwise from the positive x-axis. At every load step, a numerical tolerance of 10^{-3} for displacements, and 10^{-2} for forces, were used as the convergence criteria for the Newton-Raphson method. Fig. 6 illustrates the initial and final deformed configurations of the riser during the static analysis.

The final static equilibrium configuration was set as the initial configuration for the dynamic simulations and all static loads were held constant. The prescribed harmonic motions, given in Table 3, were applied at the riser's top connection. The amplitude of the prescribed motions was gradually increased according to a sinusoidal function, during the first two loading periods (i.e., 26.484 s), to minimize the transient axial vibrations. The total simulation time was set as 70 s and a time step of 0.01 s was used. The HHT method [29] was employed to integrate the differential equations of motion with an alpha parameter of 0.1.

During the dynamic analysis, a periodic reduction in the radii of curvature was observed. Fig. 7(a), (b), and (c) illustrate the minimum values of the radius of curvature along the riser length for three critical time intervals: 30–37s, 43–50s, and 57–63s, respectively. The gray region in Fig. 7 corresponds to the critical section of the riser with the smallest radii of curvature and, therefore, the greatest values of the bending moments (in the FEM model, this section of the riser is $399\,m$ long and is located between nodes 832 and 965). To address the effects of the small radius of curvature,

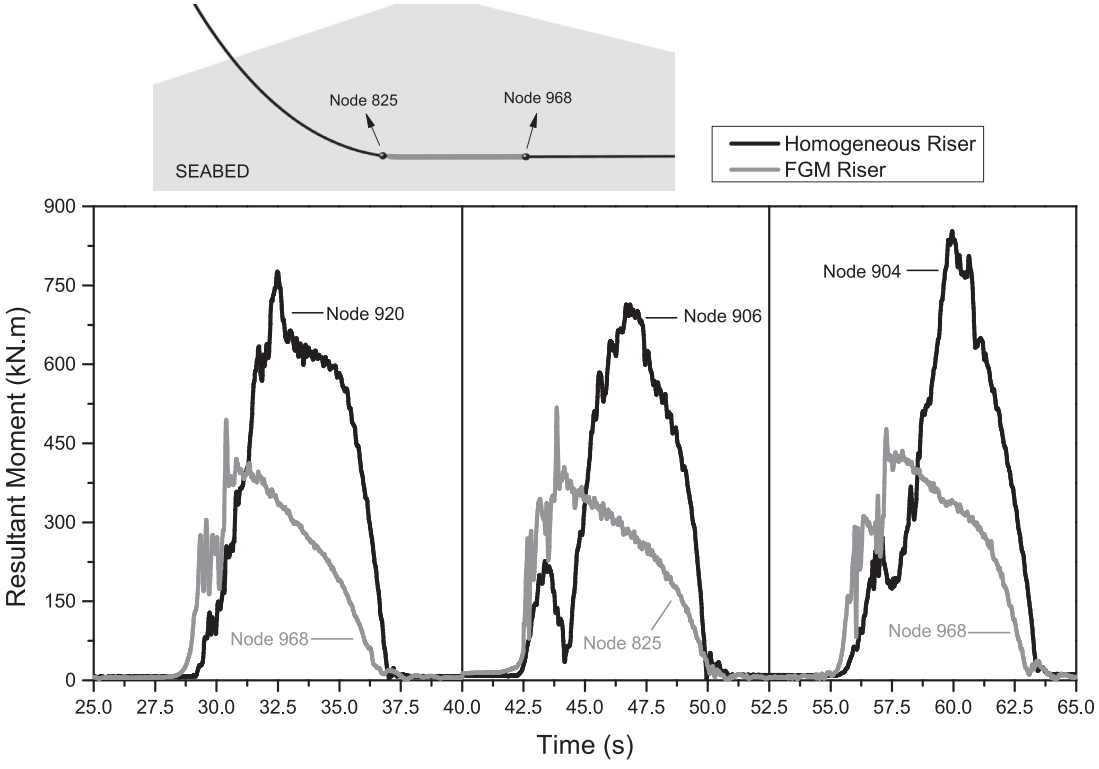

Fig. 9. Resultant bending moment in co-rotated local system (near TDZ).

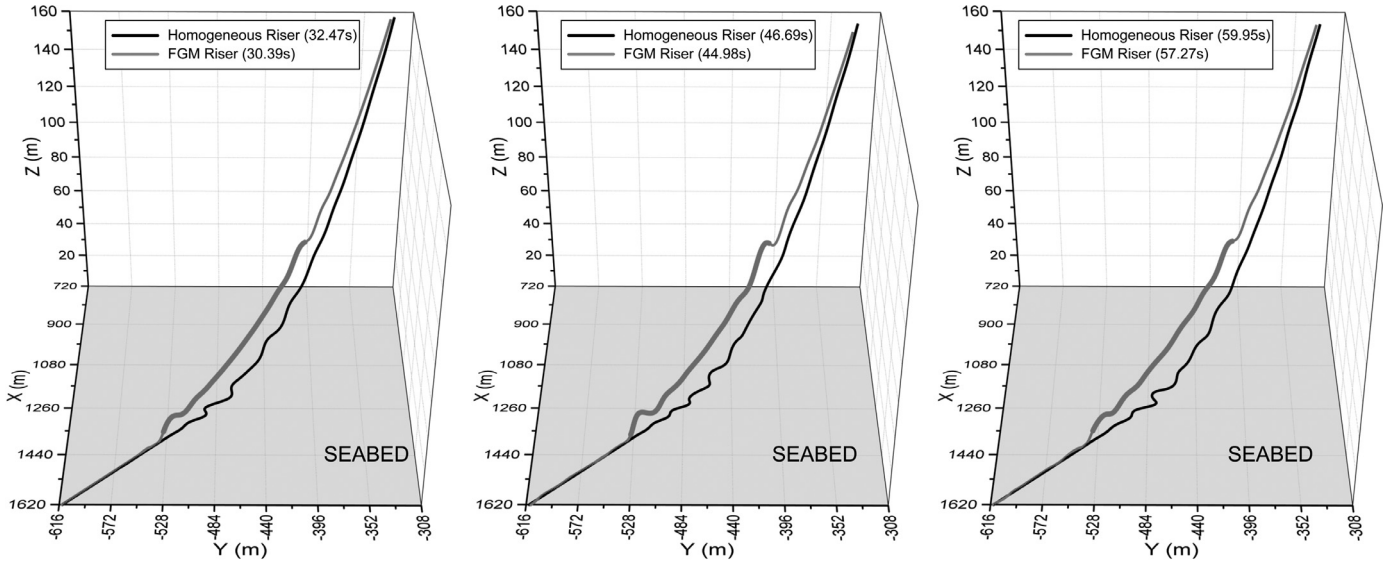

Fig. 10. Deformed configurations for homogeneous riser and FGM riser at critical time instants (near TDZ).

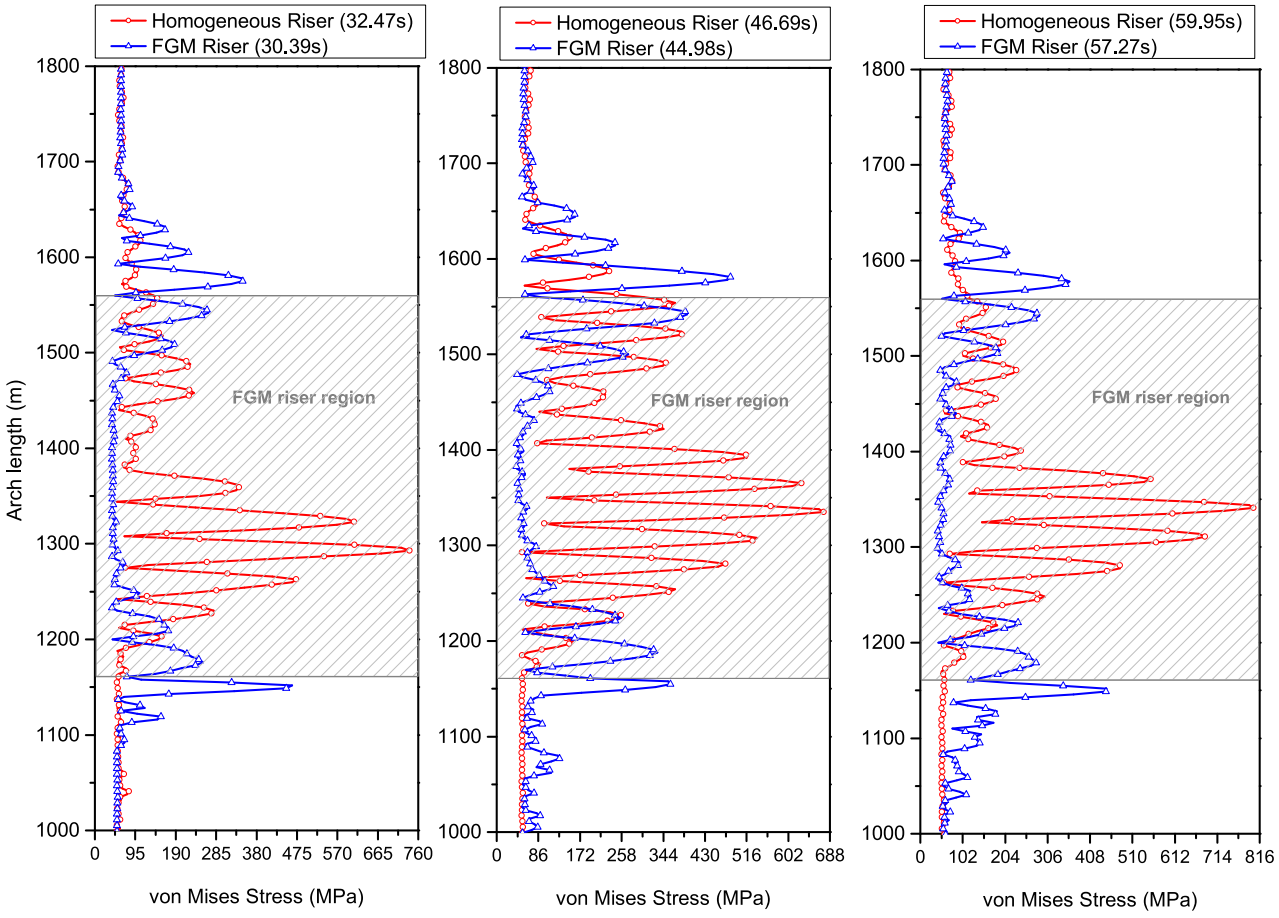

Fig. 11. von Mises stress at the internal riser radius (near TDZ).

the critical section of the riser was replaced by a Ni_3Al-TiC (Nickel Aluminide/ Titanium Carbide) FGM riser, with Ni_3Al and TiC phases in the internal and external radius, respectively. The power laws for the modulus of elasticity and specific weight of the FGM are given in Table 1. It is important to mention that the critical section of the riser, where the FGM was placed, encompassed the TDZ and, in addition to small radii of curvature, this region was subjected to the greatest amplitude variation of the axial forces (i.e., from tension to compression), as depicted in Fig. 8, for a typical node of each riser (homogeneous and FGM). Both static and dynamic analyses were performed considering the new FGM riser, following the same approach described previously for the homogeneous riser. The results obtained with the FGM riser indicate a significant increase in the radii of curvature (see blue curves in Fig. 7(a),

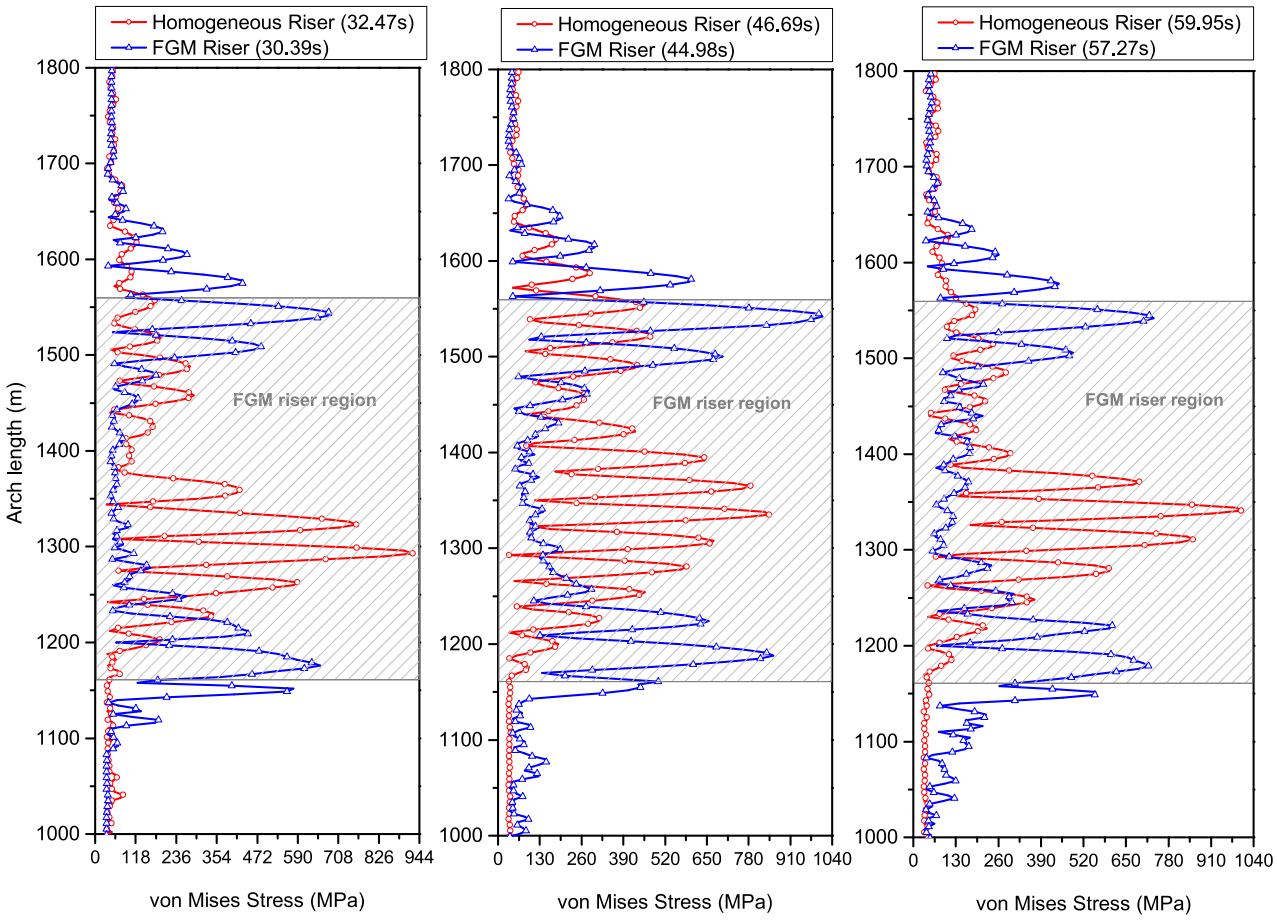

Fig. 12. von Mises stress at the external riser radius (near TDZ).

(b), and (c)). Table 4 presents the minimum values of the radius of curvature, for both risers, considering the same time intervals indicated in Fig. 7. Notice that the use of FGM increased the radii of curvature, in each time interval, by approximately 55.4%, 42.3%, and 72.1%, respectively. However, we acknowledge that this is a preliminary study and thus further investigation is needed.

Table 5 displays the nodes of each riser that experienced the minimum value of the radius of curvature and Fig. 9 illustrates the corresponding values of the resultant bending moments in each time interval. The results obtained herein demonstrate a significant reduction in the values of bending moments for the FGM riser compared to the homogeneous riser. Fig. 10 illustrates the deformed configurations of the risers corresponding to the critical time instants, i.e., the times when the bending moments achieved their maximum values (according to Fig. 9). It is important to mention that, for the FGM case, the deformation of the riser, specifically in the region near the TDZ, was limited to the catenary's plane, thereby reducing and redistributing the overall stresses in this region.

Figs. 11 and 12 display a comparison between the FGM and homogeneous risers with respect to the envelope of maximum von Mises stresses in the region near the TDZ. A significant reduction in the values of von Mises stresses is observed in the FGM riser. Considering that a conventional homogeneous riser is made of Carbon Steel API 5L X70 (whose yield strength is equal to 482.6 MPa), this material could fail. Conversely, the Ni_3Al-TiC FGM riser, although subjected to a high level of stresses in the external radius, can be designed with a higher flexural strength depending on the parameters for the melt infiltration process and volume fraction of Ni_3Al. Therefore, the flexural strength at 22^oC for a Ni_3Al-TiC composite fabricated using a simple melt infiltration, prepared at $1300^\circ C$ and with 20 vol%Ni_3Al, could achieve a level of 1080 MPa [34].

5. Concluding remarks

In this study, the use of FGMs at critical regions of an SCR, such as the TDZ, proved to be an effective procedure in reducing dynamic effects. This idea can also be applied to other riser configurations to improve their dynamic behavior. The results from this work confirm that FGM risers are an acceptable alternative for deep-water applications under extreme loading conditions.

It is also important to highlight that the use of FGM risers can address technological challenges beyond their dynamic behavior. As FGMs combine thermal insulation and corrosion-resistance characteristics of ceramics with the mechanical strength and hardness of metals, they are promising materials to be used in Brazil's deep-water pre-salt fields, where materials are required to withstand the high pressures and corrosion associated with the CO_2 and H_2S produced. Therefore, further studies are encouraged to verify the viability of FGM risers to address such problems.

Author Contributor

All authors have participated in (a) conception and design, or analysis and interpretation of the data; (b) drafting the article or revising it critically for important intellectual content; and (c) approval of the final version.

Declaration of Competing Interest

None.

Acknowledgments

JCRA is thankful for the financial support provided by CNPq (Conselho Nacional de Desenvolvimento Científico e Tecnológico - Brazil) and the Pontifical Catholic University of Rio de Janeiro. IFMM acknowledges the support provided by CNPq, Tecgraf/PUC-Rio (Institute of Technical-Scientific Software Development), and Coordenação de Aperfeiçoamento de Pessoal de Nível Superior - Brasil (CAPES) - Finance Code 001. GHP acknowledges support from the Raymond Allen Jones Chair at the Georgia Institute of Technology.

References

[1] H. Howells, Advances in steel catenary riser design, 2nd Annual International Forum on Deepwater Technology, DEEPTEC, Feb 28 - March 2, Aberdeen, 1995.
[2] M. Yazdchi, M.A. Crisfield, Buoyancy forces and the 2D finite element analysis of flexible offshore pipes and risers, International Journal for Numerical Methods in Engineering 54 (1) (2002) 61–88.
[3] M. Yazdchi, M.A. Crisfield, Non-linear dynamic behaviour of flexible marine pipes and risers, International Journal for Numerical Methods in Engineering 54 (9) (2002) 1265–1308.
[4] S.H. Kordkheili, H. Bahai, M. Mirtaheri, An updated Lagrangian finite element formulation for large displacement dynamic analysis of three-dimensional flexible riser structures, Ocean Engineering 38 (5) (2011) 793–803.
[5] L.L. Aguiar, C.A. Almeida, G.H. Paulino, A three-dimensional multilayered pipe beam element: Nonlinear analysis, Computers & Structures 138 (2014) 142–161.
[6] A. Connaire, P. O'Brien, A. Harte, A. O'Connor, Advancements in subsea riser analysis using quasi-rotations and the Newton-Raphson method, International Journal of Non-Linear Mechanics 70 (2015) 47–62.
[7] L.L. Aguiar, C.A. Almeida, G.H. Paulino, Dynamic analysis of risers using a novel multilayered pipe beam element model, Marine Structures 44 (2015) 211–231.
[8] A.G. Neto, Dynamics of offshore risers using a geometrically-exact beam model with hydrodynamic loads and contact with the seabed, Engineering Structures 125 (2016) 438–454.
[9] J.C.R. Albino, C.A. Almeida, I.F.M. Menezes, G.H. Paulino, Co-rotational 3D beam element for nonlinear dynamic analysis of risers manufactured with functionally graded materials (FGMs), Engineering Structures 173 (2018) 283–299.
[10] J.-J. Fu, H.-Z. Yang, Fatigue characteristic analysis of deepwater steel catenary risers at the touchdown point, China Ocean Engineering 24 (2010) 291–304.
[11] F.Z. Li, Y.M. Low, Fatigue reliability analysis of a steel catenary riser at the touchdown point incorporating soil model uncertainties, Applied Ocean Research 38 (2012) 100–110.
[12] K. Wang, H. Xue, W. Tang, J. Guo, Fatigue analysis of steel catenary riser at the touch-down point based on linear hysteretic riser-soil interaction model, Ocean Engineering 68 (2013) 102–111.
[13] X. Bai, W. Huang, M.A. Vaz, Z. Yang, M. Duan, Riser-soil interaction model effects on the dynamic behavior of a steel catenary riser, Marine Structures 41 (2015) 53–76.
[14] Y. Bai, Q. Bai, Subsea Pipelines and Risers, first ed., Elsevier, 2005.
[15] R.L.C. Beltrão, C.L. Sombra, A.C.V. Lage, J.R.F. Netto, C.C.D. Henriques, Challenges and new technologies for the development of the pre-salt cluster, Santos basin, Brazil, in: Offshore Technology Conference, 4–7 May, Houston, Texas, 2009.
[16] D. Pham, S. Narayanaswamy, X. Qian, A. Sobey, M. Achintha, A. Shenoi, Composite riser design and development a review, in: C.G. Soares, R.A. Shenoi (Eds.), Analysis and Design of Marine Structures V, CRC Press, 2015, pp. 637–645.
[17] D.-C. Pham, N. Sridhar, X. Qian, A.J. Sobey, M. Achintha, A. Shenoi, A review on design, manufacture and mechanics of composite risers, Ocean Engineering 112 (2016) 82–96.
[18] G. Marinucci, A.H. Andrade, Microstructural analysis in asymmetric and un-balanced composite cylinders damaged by internal pressure, Composite Structures 72 (1) (2006) 86–90.
[19] E. Theotokoglou, Behaviour of thick composite tubes considering of delamination, Theoretical and Applied Fracture Mechanics 46 (3) (2006) 276–285.
[20] A.G. Gibson, in: The cost effective use of fibre reinforced composites offshore, Report submitted to the Health and Safety Executive, Centre for Composite Materials Engineering, University of Newcastle Upon Tyne, United Kingdom, 2003, pp. 1–140.
[21] M.R. Hill, R.D. Carpenter, G. Paulino, Z.A. Munir, J.C. Gibeling, Fracture testing of a layered functionally graded material, ASTM Special Technical Publication (2002) 169–184.
[22] D. Jha, T. Kant, R. Singh, A critical review of recent research on functionally graded plates, Composite Structures 96 (2013) 833–849.
[23] D. Karunakaran, A. Dutta, T. Clausen, K. Lund, Steel catenary riser configurations for large motion semi submersibles with lightweight coating, in: Deep Offshore Technology Conference, DOT, New Orleans, 2002.
[24] D. Karunakaran, T. Meling, S. Kristoffersen, K. Lund, Weight-optimized SCRs for deepwater harsh environments, in: Offshore Technology Conference, 2–5 May, Houston, Texas, 2005.
[25] E. Foyt, C. Griffin, M. Campbell, H.H. Wang, W.C. Kan, Weight optimized SCR enabling technology for turret moored FPSO developments, in: International Conference on Ocean, Offshore and Arctic Engineering - OMAE2007, 10–15 June, San Diego, California, 2007.
[26] J.-L. Legras, D.N. Karunakaran, R.L. Jones, Fatigue enhancement of SCRs: Design applying weight distribution and optimized fabrication, in: Offshore Technology Conference, 6–9 May, Houston, Texas, 2013.
[27] K.-J. Bathe, E. Ramm, E.L. Wilson, Finite element formulations for large deformation dynamic analysis, International Journal for Numerical Methods in Engineering 9 (2) (1975) 353–386.
[28] L. Meirovitch, Elements of Vibration Analysis, second ed., McGraw-Hill, New York, 1986.
[29] H. Hilber, T. Hughes, R. Taylor, Improved numerical dissipation for time integration algorithms in structural dynamics, Earthquake Engineering and Structural Dynamics 5 (1977) 282–292.
[30] D.M.L. Silva, F.N. Corrêa, B.P. Jacob, A generalized contact model for nonlinear dynamic analysis of floating offshore systems, in: International Conference on Ocean, Offshore and Arctic Engineering - OMAE2006, 4–9 June, Hamburg, Germany, 2006.
[31] N. Tutuncu, M. Ozturk, Exact solutions for stresses in functionally graded pressure vessels, Composites Part B: Engineering 32 (8) (2001) 683–686.
[32] S. Timoshenko, J.N. Goodier, Theory of Elasticity, third ed., McGraw-Hill, New York, 1970.
[33] C.A. Almeida, J.C.R. Albino, I.F.M. Menezes, G.H. Paulino, Geometric nonlinear analyses of functionally graded beams using a tailored Lagrangian formulation, Mechanics Research Communications 38 (8) (2011) 553–559.
[34] K.P. Plucknett, P.F. Becher, S.B. Waters, Flexure strength of melt-infiltration-processed Titanium Carbide/Nickel Aluminide composites, Journal of the American Ceramic Society 81 (7) (1998) 1839–1844.